INTERNATIONAL JOURNAL FOR NUMERICAL METHODS IN FLUIDS
Int. J. Numer. Meth. Fluids 2007; **54**:901–922
Published online 7 February 2007 in Wiley InterScience (www.interscience.wiley.com). DOI: 10.1002/fld.1443

Modelling of fluid–structure interactions with the space–time finite elements: Arterial fluid mechanics

Tayfun E. Tezduyar[1,*,†], Sunil Sathe[1], Timothy Cragin[1], Bryan Nanna[1], Brian S. Conklin[2], Jason Pausewang[1] and Matthew Schwaab[1]

[1]*Team for Advanced Flow Simulation and Modeling (T★AFSM), Mechanical Engineering, Rice University - MS 321, 6100 Main Street, Houston, TX 77005, U.S.A.*
[2]*Sections of Leukocyte Biology and Nutrition, Department of Pediatrics, Baylor College of Medicine, Children's Nutrition Research Center, 1100 Bates, Suite 6014, Houston, TX 77030, U.S.A.*

SUMMARY

The stabilized space–time fluid–structure interaction (SSTFSI) techniques developed by the Team for Advanced Flow Simulation and Modeling (T★AFSM) are applied to FSI modelling in arterial fluid mechanics. Modelling of flow in arteries with aneurysm is emphasized. The SSTFSI techniques used are based on the deforming-spatial-domain/stabilized space–time (DSD/SST) formulation and include the enhancements introduced recently by the T★AFSM to increase the scope, accuracy, robustness and efficiency of these techniques. The arterial structures can be modelled with the membrane or continuum elements, both of which are geometrically nonlinear, and the continuum element can be made of linearly elastic or hyperelastic material. Test computations are presented for cerebral and abdominal aortic aneurysms and carotid-artery bifurcation, where the arterial geometries used in the computations are close approximations to the patient-specific image-based data. Copyright © 2007 John Wiley & Sons, Ltd.

Received 1 December 2006; Revised 6 December 2006; Accepted 10 December 2006

KEY WORDS: cardiovascular fluid mechanics; cerebral aneurysms; fluid–structure interactions; finite elements; space–time methods

1. INTRODUCTION

One of the major computational challenges in cardiovascular fluid mechanics is accurate modelling of the fluid–structure interactions (FSI) between the blood flow and arterial walls. The blood flow

*Correspondence to: Tayfun E. Tezduyar, Team for Advanced Flow Simulation and Modeling (T★AFSM), Mechanical Engineering, Rice University - MS 321, 6100 Main Street, Houston, TX 77005, U.S.A.
†E-mail: tezduyar@rice.edu

Contract/grant sponsor: NIH/NHLBI; contract/grant number: HL73868
Contract/grant sponsor: USDA; contract/grant number: 6250-51000-046

depends on the arterial geometry, and the deformation of the arterial wall depends on the blood flow. The equations governing the blood flow and arterial deformation need to be solved simultaneously, with proper kinematic and dynamic conditions coupling the two physical systems. Much has been accomplished in FSI modelling research since the early 1990s (see, for example, [1–35]), and a good portion of that FSI research has been directed towards arterial fluid mechanics (see, for example, [19, 22, 36–40]).

The deforming-spatial-domain/stabilized space–time (DSD/SST) formulation [1–3, 9] was introduced by the Team for Advanced Flow Simulation and Modeling (T★AFSM)[‡] in 1991 as a general-purpose interface-tracking (i.e. moving mesh) technique for simulation of flow problems with moving boundaries or interfaces. The formulation is based on the streamline-upwind/Petrov–Galerkin (SUPG) [41, 42] and pressure-stabilizing/Petrov–Galerkin (PSPG) [1, 43] methods. An earlier version of the pressure stabilization, for Stokes flows, was introduced in [44]. The stabilized space–time formulations were introduced and tested earlier by other researchers in the context of problems with fixed spatial domains (see, for example, [45]).

The DSD/SST formulation and the mesh update methods [46–48] developed by the T★AFSM are the core technologies for the space–time FSI techniques introduced by the T★AFSM (see, for example, [4, 5, 7, 12, 15, 20, 21, 28]). These space–time FSI techniques have been used in a number of 3D FSI computations in arterial fluid mechanics (see [36–40]), emphasizing cerebral aneurysms, with the arterial models extracted from computed tomography. In those computations, because the arteries modelled have relatively large diameters, the blood was assumed to behave like a Newtonian fluid. The arterial structures were modelled with continuum elements, which were geometrically nonlinear, made of linearly elastic material. The coupled fluid and structural mechanics and mesh-moving equations were solved with a block-iterative coupling technique (see [20, 21, 49] for comparative descriptions of the block-iterative, quasi-direct and direct coupling techniques). The inflow boundary condition used in the computations is a pulsatile velocity profile, which closely represents the measured flow rate during a heartbeat cycle. We provide here a brief, chronological review of those computations.

A journal article [36] published in 2004 by the Japan Society of Mechanical Engineers is where arterial fluid mechanics computations with the space–time FSI techniques introduced by the T★AFSM were first reported. Segments of two different middle cerebral arteries with aneurysm were modelled—a single-artery segment from a 57-year-old male and a bifurcating-artery segment from a 59-year-old female. The FSI computations showed that taking the arterial-wall deformation into account significantly influences the calculation of the haemodynamic factors, including the wall shear stress (WSS) distribution. FSI modelling of a segment of the internal carotid artery of a male patient in his 70s was reported first in a conference paper [37]. The computations showed the importance of taking into account the FSI between the blood flow and the arterial walls of a sharply curved artery. The journal version of the material reported in [37] was presented in [38]. Modelling of the FSI and WSS for aneurysmal conditions with high blood pressure was reported in a journal article [39]. The cerebral-artery segment modelled was the same as the bifurcating-artery segment modelled in [36]. The computations showed that hypertension makes a significant difference in the predicted values of not only the mechanical stress in the aneurysmal wall but also the WSS.

[‡]This team name was intended to imply the research team led by Tezduyar also prior to when the team assumed this specific name.

DOI: 10.1002/fld

The material presented in [40] (a journal article) is a translated, revised and expanded version of what was reported in [36].

New, enhanced versions of the DSD/SST and space–time FSI techniques were recently introduced in [49] to increase the scope, accuracy, robustness and efficiency of these techniques. In these new versions, the aspects of the FSI solution process that were enhanced include the DSD/SST formulation, the fluid–structure interface conditions, the preconditioning techniques used in iterative solution of the linear equation systems, and a contact algorithm protecting the quality of the fluid mechanics mesh between the structural surfaces coming into contact. A number of 3D numerical examples computed with these new stabilized space–time FSI (SSTFSI) techniques were also presented in [49]. Our objective in this paper, which is for all practical purposes a continuation of [49], is to extend the new SSTFSI techniques to FSI modelling in arterial fluid mechanics. The structural modelling for the arteries can be based on the membrane or continuum elements, both of which are geometrically nonlinear, and the continuum element can be made of linearly elastic or hyperelastic (Mooney–Rivlin) material. The test computations we will be presenting in this paper are for cerebral and abdominal aortic aneurysms and carotid-artery bifurcation, where the arterial geometries used in the computations are close approximations to the patient-specific image-based data. In computations involving cerebral aneurysms, the arterial geometries are close approximations to the geometries used in the computations described in the preceding paragraph. However, it is not our objective to conduct arterial fluid mechanics studies at a level of detail seen in the papers cited in the preceding paragraph. Our objective is to test the new SSTFSI techniques on arterial fluid mechanics computations and show that these techniques can successfully deal with different types of arterial problems and structural models.

Because this paper is essentially a continuation of [49], we only provide here the mathematical models and computational techniques that go beyond those described in [49]. These additional topics are basically related to the structural modelling of the arteries, covered in Section 2. General conditions for the test computations are given in Section 3, and the test computations themselves are presented in Section 4. The concluding remarks are given in Section 5.

2. STRUCTURAL MODELS FOR THE ARTERIES

The governing equations for the structural model, the corresponding finite element formulation, and how that formulation couples with the rest of the FSI system remain the same as they were given in [49]. For the arterial structural models we cover here, what makes one structural element model different from the other is the manner in which the second Piola–Kirchoff stress tensor $\mathbf{S}$ is defined.

2.1. Membrane element

For the membrane element, the expression for $\mathbf{S}$ is given in Section 2.2 of [49].

2.2. Continuum element

2.2.1. Linearly elastic material. For the continuum element made of linearly elastic material, the expression for $\mathbf{S}$ is given as

$$S^{ij} = (\lambda^s G^{ij} G^{kl} + \mu^s (G^{il} G^{jk} + G^{ik} G^{jl})) E_{kl} \tag{1}$$

DOI: 10.1002/fld

where λ^s and μ^s are the Lamé constants, G^{ij} are the contravariant components of the metric tensor in the original configuration, and E_{kl} are the components of the Cauchy–Green strain tensor.

2.2.2. Hyperelastic (Mooney–Rivlin) material. For the continuum element made of hyperelastic (Mooney–Rivlin) material, the expression for $\mathbf{S}$ is given as

$$S^{ij} = 2(C_1 + C_2 G^{kl} g_{kl}) G^{ij} - 2C_2 G^{ik} g_{kl} G^{lj} + (K_{\mathrm{PEN}} \ln(\sqrt{I_3}) - 2(C_1 + 2C_2)) g^{ij} \tag{2}$$

where C_1 and C_2 are the Mooney–Rivlin material constants, and g_{kl} and g^{ij} are the covariant and contravariant components of the metric tensor in the deformed configuration. The incompressibility constraint is enforced with the penalty term $K_{\mathrm{PEN}} \ln(\sqrt{I_3})$ (see [50]). Here I_3 is the third invariant of the Green–Lagrange strain tensor, and K_{PEN} is a penalty parameter determined based on the expression given in [51] for the bulk modulus:

$$K_{\mathrm{PEN}} = \frac{2(C_1 + C_2)}{(1 - 2\nu_{\mathrm{PEN}})} \tag{3}$$

where ν_{PEN} (with a value close to 0.50) is the 'penalty' Poisson's ratio we use in the expression in place of the actual Poisson's ratio.

3. GENERAL CONDITIONS FOR THE TEST COMPUTATIONS

All computations were carried out in a parallel computing environment, using PC clusters. The meshes were generated on a single node of the cluster used. In all cases computed, the fluid and structure meshes are compatible at the fluid–structure interface. All computations were completed without any remeshing. In all cases, the fully discretized, coupled fluid and structural mechanics and mesh-moving equations were solved with the quasi-direct coupling technique (see Section 5.2 in [49]). In solving the linear equation systems involved at every nonlinear iteration, the GMRES search technique [52] was used with a diagonal preconditioner.

3.1. Fluid and structure properties

As it was done for the computations reported in [36–40], the blood is assumed to behave like a Newtonian fluid. The density and kinematic viscosity are set to $1000\,\mathrm{kg/m^3}$ and $4.0 \times 10^{-6}\,\mathrm{m^2/s}$. The material density of the arterial wall is known to be close to that of the blood and therefore set to $1000\,\mathrm{kg/m^3}$. The stiffness values used for the arteries are comparable to those used in [36–40], where the values used were determined (see [40]) by comparison to experimental values. The stiffness value used in each test case is given in the individual description of that test case. Arteries are surrounded by tissues, and we expect those tissues to have a damping effect on the structural dynamics of the arteries. Therefore, we add a mass-proportional damping, which also helps in removing the high-frequency modes of the structural deformation. The damping coefficient η used in each case is given in the individual description of that case.

3.2. Boundary conditions

In all the test cases computed, we have a single inflow boundary where we specify the velocity profile as a function of time. The profile is similar to the one obtained by using the Womersley

DOI: 10.1002/fld

solution of a pulsating flow [53]. At the outflow boundaries, we specify traction boundary conditions. In test cases with two outflow boundaries, we specify the same condition for both. The traction boundary condition is based on the pressure profile applicable to the case computed. The pressure profile, as a function of time, is obtained from an approximate solution [38] of the Windkessel model [54]. The parameters in the Windkessel model are set in such a way that the range for the pressure profile is approximately from 80 to 120 mmHg for normal blood pressure (NBP) and from 100 to 170 mmHg for high blood pressure (HBP). On the arterial walls, we specify no-slip boundary conditions for the flow. In the structural mechanics part, as boundary condition at the ends of the arteries, we set the displacement to zero at those edges (for the membrane elements) and faces (for the continuum elements).

3.3. Simulation sequence

In most of the simulations carried out by the T⋆AFSM, the FSI computations are preceded by a set of pre-FSI computations that provide us a good starting point for the FSI computations. These pre-FSI computations include the fluid-only and structure-only computations. We have two options for the pre-FSI generation of the fluid mesh. We can generate it by starting with a mesh corresponding to the initial shape of the structure and updating it as the structure-only computation proceeds or generate it after the structure-only computation is completed. We built two simulation sequences that were used in the computations reported here. Our experience with the first one helped us design the second one.

3.3.1. Fluid → structure → FSI (F → S → FSI) sequence.

Step 1: Generate the fluid and structure meshes based on the shape of the unstressed structure.
Step 2: Compute a developed flow field while holding the structure rigid.

- The outflow traction is set to a value close to 80 mmHg for NBP and 100 mmHg for HBP.
- The inflow velocity is set to a value corresponding to the outflow traction.

Step 3: Compute the structural deformation, with the fluid stresses at the interface held steady at their values from Step 2, and simultaneously update the fluid mesh.

- Structural deformation can be determined with a steady-state computation or a time-dependent computation that eventually yields a steady-state solution.
- For the steady-state computation, $\Delta t \to \infty$ and $\alpha = 0$ in Equation (21) in [49], the number of time steps is one, and the initial displacement, velocity and acceleration are set to zero.
- The mesh quality obtained with the time-dependent computation is better than the one obtained with the steady-state computation.

Step 4: Compute the FSI with the inflow and outflow conditions held steady at the values used in Step 2.

- Sometimes, to prevent a sudden increase in the structural acceleration at the start of this step, it may be necessary to begin with an increased structural mass that would later be decreased back to its actual value. An unrealistically large acceleration can initiate an instability that is subsequently magnified.

Step 5: Compute the FSI with the inflow and outflow conditions pulsating.

DOI: 10.1002/fld

3.3.2. Structure → fluid → FSI (S → F → FSI) sequence. Analysis of the results obtained with the F → S → FSI sequence revealed that the fluid pressure is spatially almost uniform. Even when the outflow traction is pulsating, although the pressure changes as a function of time, spatially it remains nearly uniform. The S → F → FSI sequence was built based on these considerations.

Step 1: Generate the structure mesh based on the shape of the unstressed structure.

Step 2: Compute the structural deformation with a uniform fluid pressure held steady at a value close to 80 mmHg for NBP and 100 mmHg for HBP:

- The structural deformation can be computed, as it was done in Step 3 of the F → S → FSI sequence, with a steady-state computation or a time-dependent computation that eventually yields a steady-state solution.

Step 3: Generate the fluid mesh based on the shape of the deformed structure.

Step 4: Compute a developed flow field while holding the structure from Step 3 rigid.

- The outflow traction is set to a value close to 80 mmHg for NBP and 100 mmHg for HBP.
- The inflow velocity is set to a value corresponding to the outflow traction.

Step 5: Continue from Step 4 of the F → S → FSI sequence.

4. TEST COMPUTATIONS

4.1. Middle cerebral artery with aneurysm—single-artery segment

The arterial geometry used is a close approximation to the patient-specific image-based geometry used in [40]. The geometry used in [40] was extracted from the computed tomography model of a segment of the middle cerebral artery of a 57-year-old male with aneurysm. The diameter and length of the artery are 3.0 and 15 mm, and the size of the aneurysm is 6 mm. The volumetric inflow rate used is also a close approximation to the one used in [40], which can be found in [38, 39]. The problem geometry and the pulsating inflow velocity profile as a function of time are shown in Figures 1 and 2.

4.1.1. Computations with the membrane element. Test computations are carried out for NBP and HBP in an artery segment with uniform and variable wall thickness (UWT and VWT). Figure 3 shows the NBP and HBP profiles, which were calculated in the way described in Section 3.2. The traction condition at the outflow boundary is based on these pressure profiles. Figure 4 shows the wall-thickness distribution for the artery segment with variable wall thickness. In all four cases (NBP-UWT, NBP-VWT, HBP-UWT and HBP-VWT), the wall thickness, stiffness and Poisson's ratio for the artery are 0.3 mm, 5.0×10^5 N/m^2 and 0.45, respectively. The wall thickness for the aneurysm is 0.3 mm for the UWT cases and 0.1 mm for the VWT cases.

The mesh for the artery consists of 3726 nodes and 7388 three-node triangular elements. The fluid mechanics mesh contains 10 987 nodes and 53 645 four-node tetrahedral elements. The computations are carried out with the SSTFSI-TIP1 technique (see Remarks 5 and 10 in [49]) and the SUPG test function option WTSA (see Remark 2 in [49]). The stabilization parameters used are those given by Equations (7)–(13) in [49] for the NBP-UWT case and Equations (7)–(12) and (17) in [49] for all other cases. The damping coefficient η is set to 6.0×10^3 s^{-1}. The time-step size is 3.333×10^{-3} s. The number of nonlinear iterations per time step is 5, and the number

DOI: 10.1002/fld

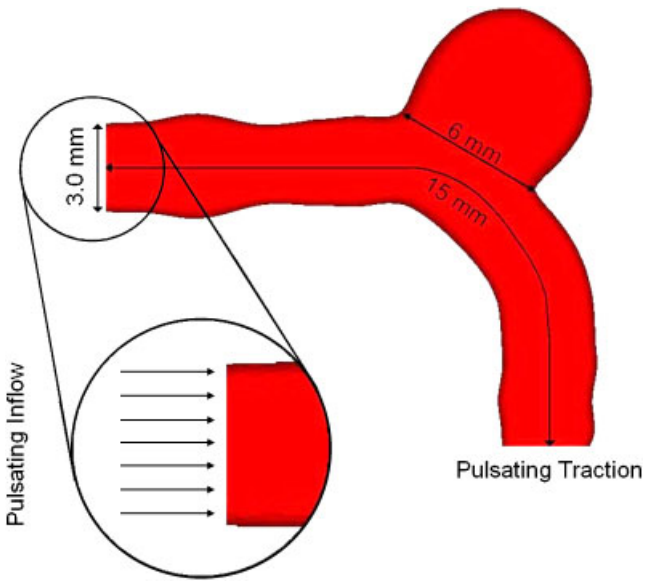

Figure 1. Middle cerebral artery with aneurysm—single-artery segment. Problem geometry.

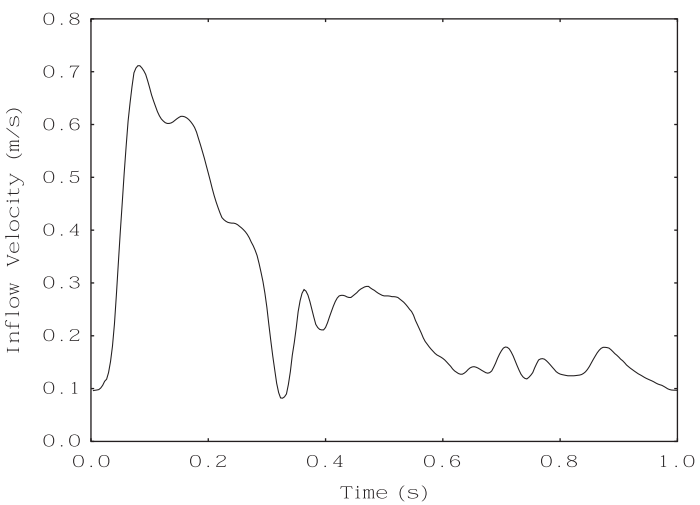

Figure 2. Middle cerebral artery with aneurysm—single-artery segment. Pulsating inflow velocity.

of GMRES iterations per nonlinear iteration is 150 and 225 for the NBP and HBP cases. The $F \rightarrow S \rightarrow FSI$ sequence is used in the computations.

Figure 5 shows the deformed shapes of the aneurysm for all four cases. The order of the cases from minimum to maximum deformation is NBP-UWT, HBP-UWT, NBP-VWT and HBP-VWT. In all four cases we achieve good mass balance. We verify the mass balance by comparing the

DOI: 10.1002/fld

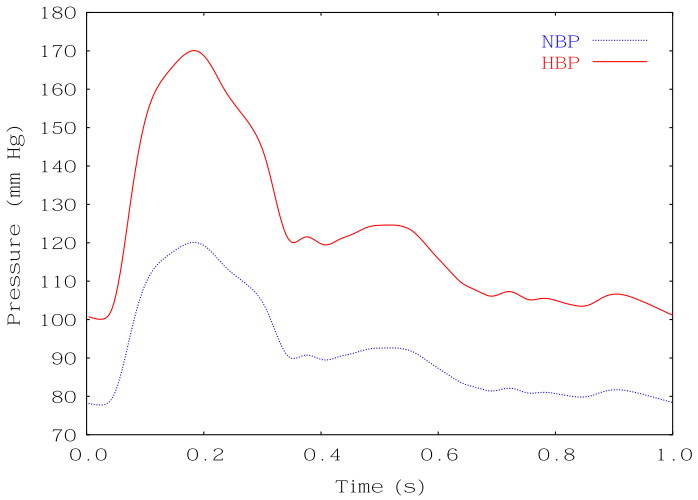

Figure 3. Middle cerebral artery with aneurysm—single-artery segment. Normal and high blood pressure (NBP and HBP) profiles.

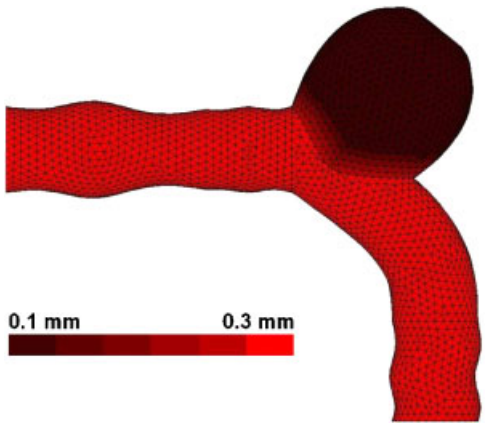

Figure 4. Middle cerebral artery with aneurysm—single-artery segment. Wall-thickness distribution for the artery segment with variable wall thickness (VWT).

rate of change for the artery volume and the difference between the volumetric inflow and outflow rates. Figure 6 shows the mass balance for the NBP-UWT case. In all four cases, we see a significant circulation inside the aneurysm. Figure 7 shows the flow field at various instants for the NBP-UWT case.

4.1.2. Computations with the continuum elements. Test computations with the continuum element are carried out for both linearly elastic and hyperelastic (Mooney–Rivlin) materials. The traction condition at the outflow boundary is based on the NBP profile shown in Figure 3 in Section 4.1.1.

DOI: 10.1002/fld

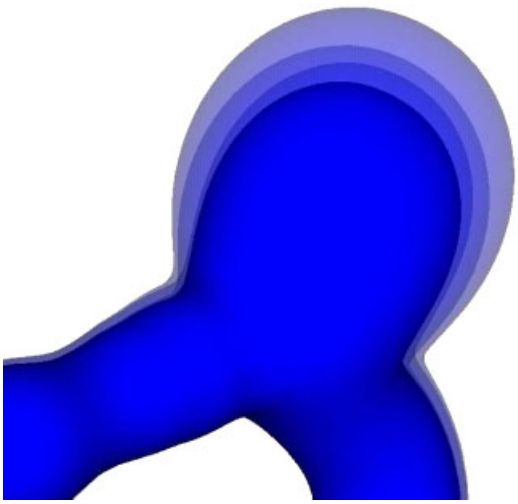

Figure 5. Middle cerebral artery with aneurysm—single-artery segment. Computed with the membrane element. Deformation of the aneurysm for all four cases. The order of the cases from minimum to maximum deformation is NBP-UWT, HBP-UWT, NBP-VWT and HBP-VWT.

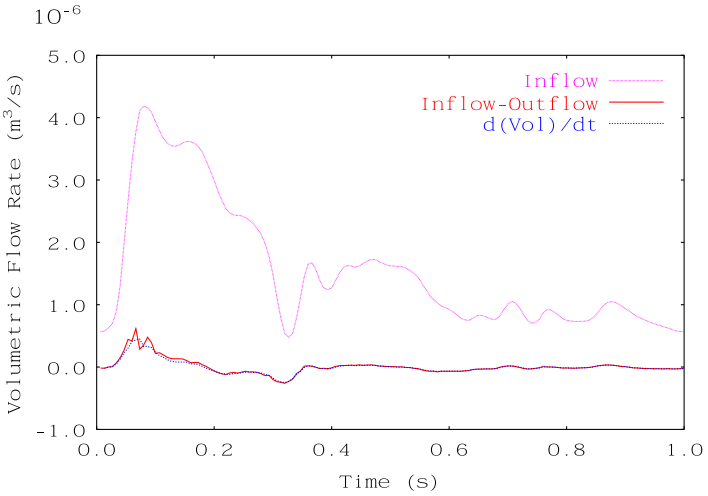

Figure 6. Middle cerebral artery with aneurysm—single-artery segment. Computed with the membrane element. Verification of mass balance for the NBP-UWT case. Volumetric inflow rate, difference between the volumetric inflow and outflow rates and rate of change for the artery volume.

The wall thickness for the artery is 0.3 mm. For the linearly elastic material, the stiffness and Poisson's ratio are $5.0 \times 10^5\,\mathrm{N/m^2}$ and 0.45. For the hyperelastic material, the Mooney–Rivlin material constants C_1 and C_2 and the penalty Poisson's ratio are 4.762×10^4, $3.571 \times 10^5\,\mathrm{N/m^2}$ and 0.45, respectively.

DOI: 10.1002/fld

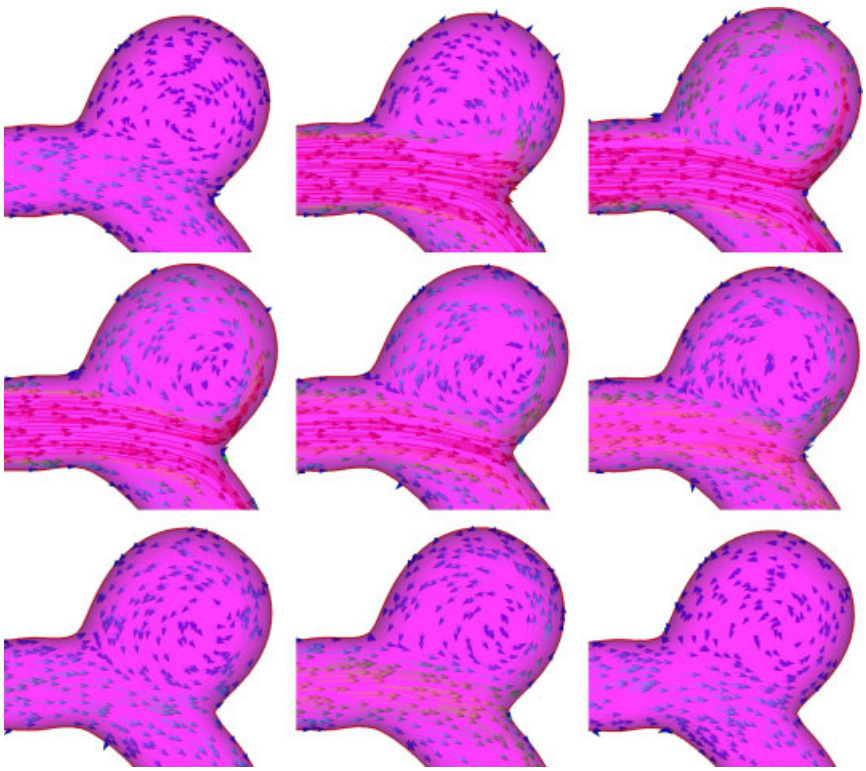

Figure 7. Middle cerebral artery with aneurysm—single-artery segment. Computed with the membrane element. Flow field at various instants for the NBP-UWT case. Velocity vectors coloured by magnitude.

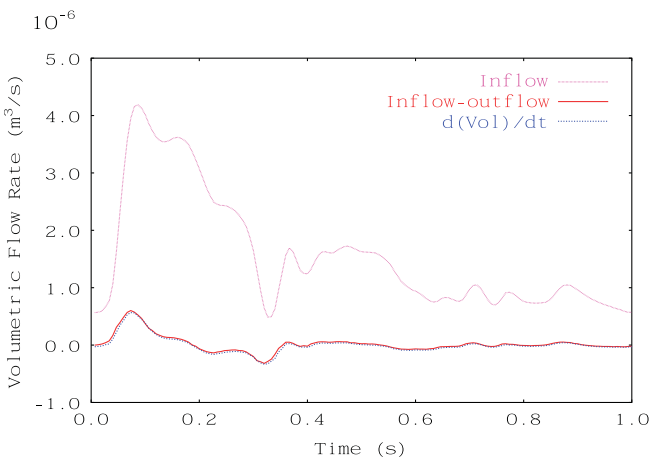

Figure 8. Middle cerebral artery with aneurysm—single-artery segment. Computed with the continuum element made of linearly elastic material. Verification of mass balance. Volumetric inflow rate, difference between the volumetric inflow and outflow rates and rate of change for the artery volume.

DOI: 10.1002/fld

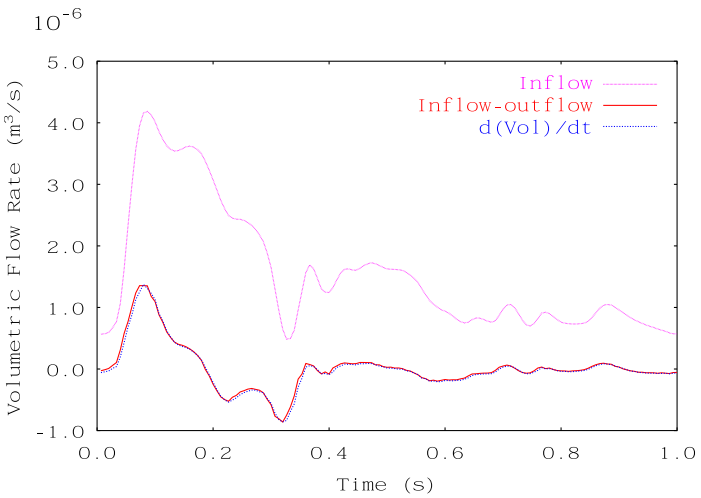

Figure 9. Middle cerebral artery with aneurysm—single-artery segment. Computed with the continuum element made of hyperelastic (Mooney–Rivlin) material. Verification of mass balance. Volumetric inflow rate, difference between the volumetric inflow and outflow rates and rate of change for the artery volume.

The mesh for the artery consists of 13 332 nodes and 52 944 four-node tetrahedral elements, with 4444 nodes and 8824 three-node triangular elements on the fluid–structure interface. The fluid mechanics mesh contains 9568 nodes and 43 960 four-node tetrahedral elements. The computations are carried out with the SSTFSI-SV technique (see Remarks 6 and 10 in [49]) and the SUPG test function option WTSE (see Remark 2 in [49]). The stabilization parameters used are those given by Equations (9)–(12) and (14)–(17) in [49]. The damping coefficient η is set to $1.5 \times 10^4\,\mathrm{s}^{-1}$. We note that, compared to the membrane element, a higher damping coefficient is used with the continuum elements because they have a different stiffness in the structural model. The time-step size is 3.333×10^{-3} s. The number of nonlinear iterations per time step is 7, and the number of GMRES iterations per nonlinear iteration is 200.

We use the 'Selective Scaling' technique (see Remark 14 in [49]) to dynamically shift the emphasis between the fluid and structure parts. The scales used for the fluid and structure parts at each nonlinear iteration of a time step are given below:

Iteration 1: fluid scale = 1.00, structure scale = 0.00.
Iteration 2: fluid scale = 0.00, structure scale = 1.00.
Iteration 3: fluid scale = 1.00, structure scale = 0.00.
Iterations 4–7: fluid scale = 1.00, structure scale = 0.01.

The scales used in the first three nonlinear iterations reduce the fluid–structure coupling to block-iterative coupling (see Section 5.1 in [49]). This allows the individual parts to converge significantly in the early stages of the iterations. The scales used in the subsequent nonlinear iterations maintain the quasi-direct coupling technique, while emphasizing the fluid part, which is found to be in more need of emphasis in these computations. The F → S → FSI sequence is used in the computations.

For both the linearly elastic and hyperelastic cases we achieve good mass balance. Figures 8 and 9 show the mass balance for those cases. We note that the deformation is larger for the hyperelastic

DOI: 10.1002/fld

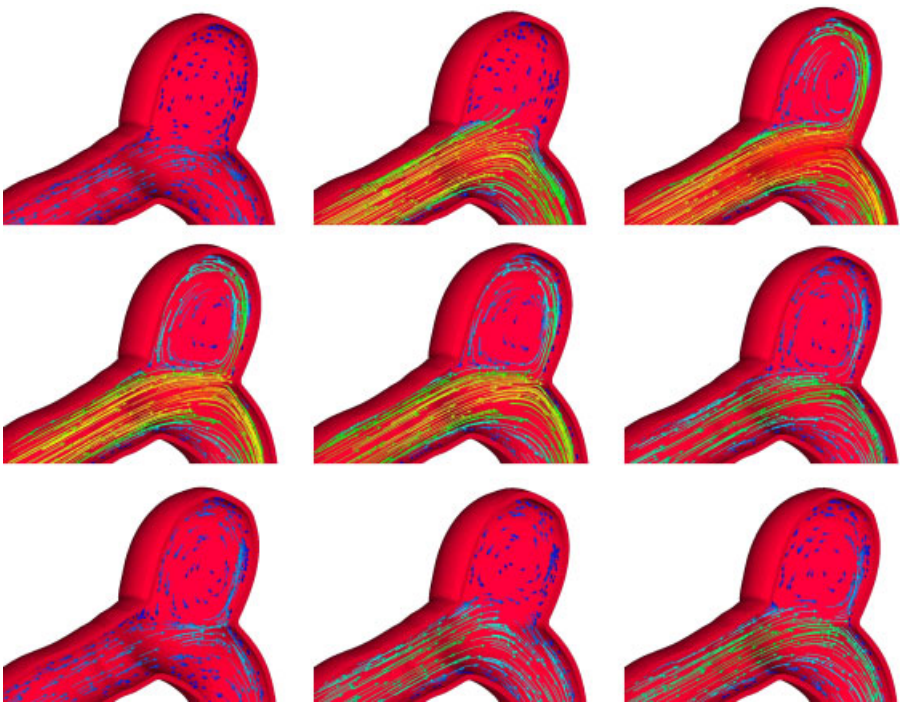

Figure 10. Middle cerebral artery with aneurysm—single-artery segment. Computed with the continuum element made of linearly elastic material. Flow field at various instants. Velocity vectors coloured by magnitude.

case. This difference and how the Mooney–Rivlin material constants should be selected need further investigation. Figures 10 and 11 show the flow field for the linearly elastic and hyperelastic cases at various instants.

4.2. Middle cerebral artery with aneurysm—bifurcating-artery segment

The arterial geometry used is a close approximation to the patient-specific image-based geometry used in [39, 40]. The geometry used in [39, 40] was extracted from the computed tomography model of a segment of the middle cerebral artery of a 59-year-old female with aneurysm. The diameter of the artery segment is 3.0 mm at the inflow, and 2.4 and 1.8 mm at the two outflow ends. The problem geometry is shown in Figure 12. The volumetric inflow rate used is also a close approximation to the one used in [39, 40], which can be found in [38, 39]. The pulsating inflow velocity profile as a function of time is the same as that shown in Figure 2 in Section 4.1. The traction condition at the outflow boundary is based on the NBP profile shown in Figure 3 in Section 4.1.1. The structural model is based on the membrane element. The wall thickness, stiffness and Poisson's ratio for the artery are 0.3 mm, $5.0 \times 10^5\,\mathrm{N/m^2}$ and 0.45, respectively.

The mesh for the artery consists of 6119 nodes and 12 150 three-node triangular elements. The fluid mechanics mesh contains 14 410 nodes and 66 440 four-node tetrahedral elements. The computations are carried out with the SSTFSI-TIP1 technique (see Remarks 5 and 10 in [49]) and the SUPG test function option WTSA (see Remark 2 in [49]). The stabilization parameters used

DOI: 10.1002/fld

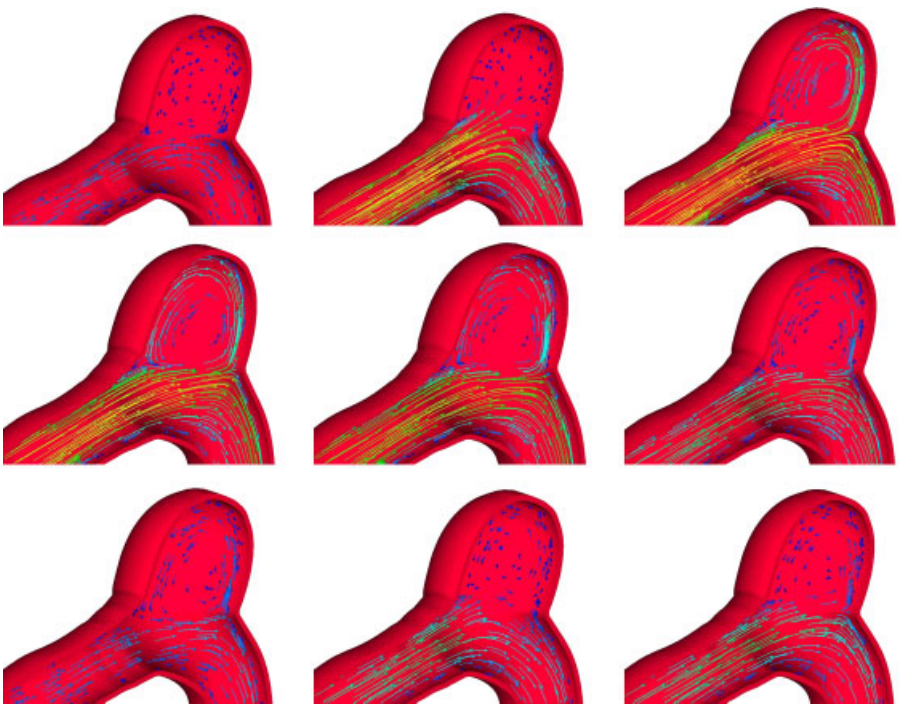

Figure 11. Middle cerebral artery with aneurysm—single-artery segment. Computed with the continuum element made of hyperelastic (Mooney–Rivlin) material. Flow field at various instants. Velocity vectors coloured by magnitude.

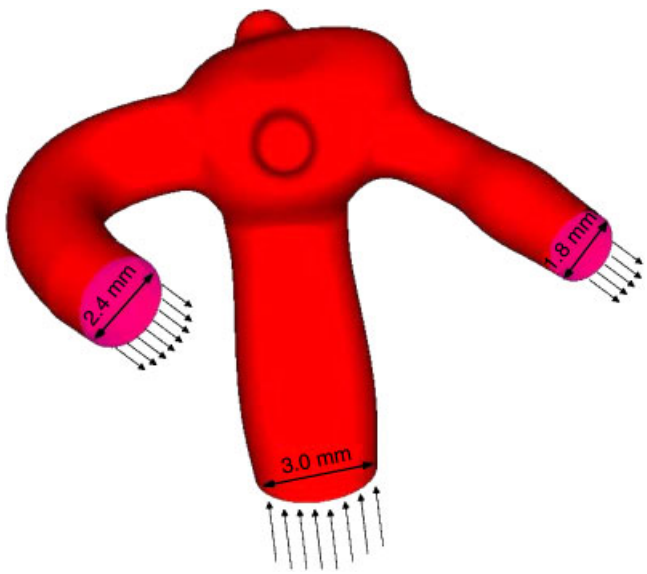

Figure 12. Middle cerebral artery with aneurysm—bifurcating-artery segment. Problem geometry.

DOI: 10.1002/fld

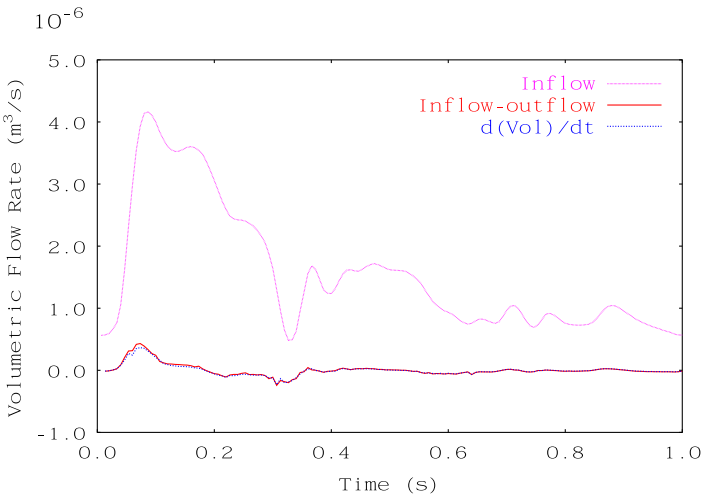

Figure 13. Middle cerebral artery with aneurysm—bifurcating-artery segment. Verification of mass balance. Volumetric inflow rate, difference between the volumetric inflow and outflow rates and rate of change for the artery volume.

are those given by Equations (7)–(12) and Equation (17) in [49]. The damping coefficient η is set to $6.0 \times 10^3\ \mathrm{s}^{-1}$. The time-step size is 6.666×10^{-3} s. The number of nonlinear iterations per time step is 5, and the number of GMRES iterations per nonlinear iteration is 150. The $\mathrm{F} \rightarrow \mathrm{S} \rightarrow \mathrm{FSI}$ sequence is used in the computations. Figure 13 shows the mass balance and Figure 14 shows the flow field at various instants.

4.3. Carotid-artery bifurcation

The arterial geometry used is an approximation to the image-based geometry found in [55], with the arterial diameter approximated from [56] and the wall thickness coming from [57]. The length of the artery segment is 36 mm. The diameter is 4.5 mm at the inflow end, 3.0 and 3.3 mm at the two outflow ends, and 5 mm at the carotid sinus. The problem geometry is shown in Figure 15. The pulsating inflow velocity profile as a function of time is not shown here but has the same form as that shown in Figure 2 in Section 4.1. The minimum and maximum values are 0.1 and 0.8 m/s. The maximum value is based on the data found in [58]. The traction condition at the outflow boundaries is based on a NBP profile calculated in the way described in Section 3.2. That pressure profile is similar to the NBP profile given in Figure 3 in Section 4.1.1. The structural model is based on the membrane element. The wall thickness, stiffness and Poisson's ratio for the artery are 0.85 mm, $5.0 \times 10^5\ \mathrm{N/m}^2$ and 0.45, respectively.

The mesh for the artery consists of 4943 nodes and 9798 three-node triangular elements. The fluid mechanics mesh contains 23 392 nodes and 131 052 four-node tetrahedral elements. The computations are carried out with the SSTFSI-SV technique (see Remarks 6 and 10 in [49]) and the SUPG test function option WTSE (see Remark 2 in [49]). The stabilization parameters used are those given by Equations (9)–(12) and (14)–(17) in [49]. The damping coefficient η is set to $8.1 \times 10^3\ \mathrm{s}^{-1}$. The time-step size is 3.7×10^{-3} s. The number of nonlinear iterations per time step is 5, and the number of GMRES iterations per nonlinear iteration is 300. We use the 'Selective

DOI: 10.1002/fld

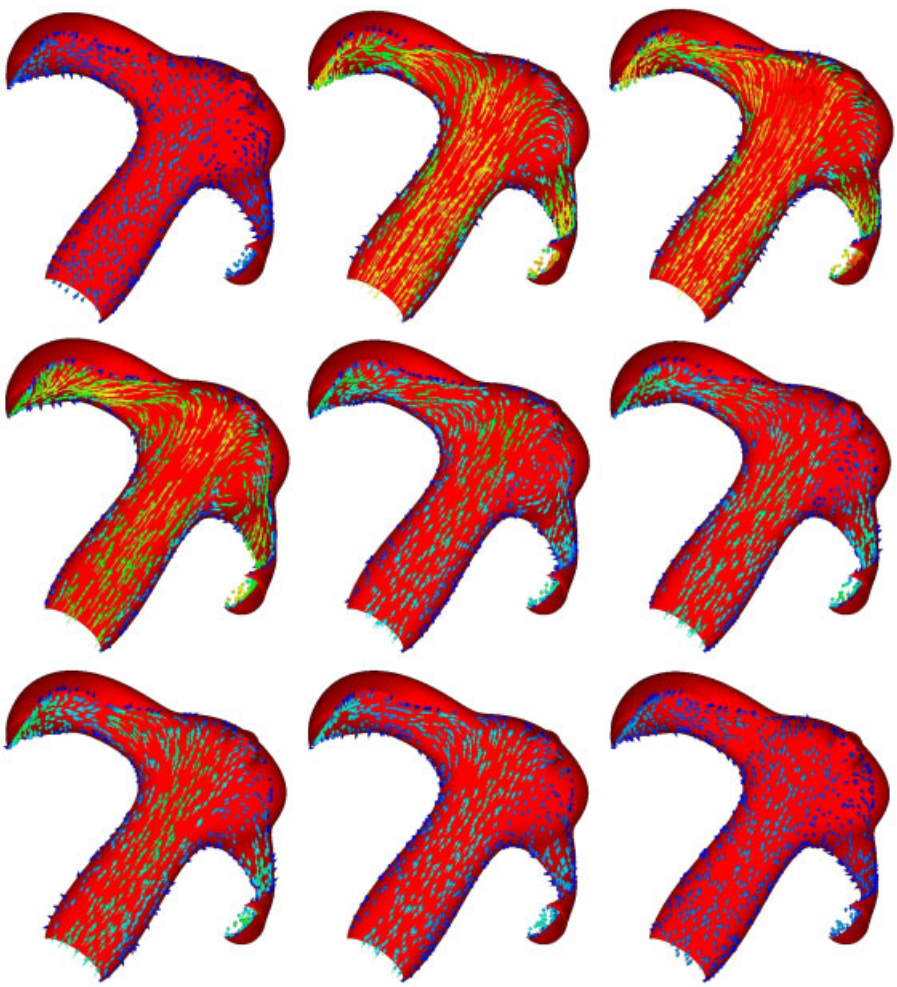

Figure 14. Middle cerebral artery with aneurysm—bifurcating-artery segment. Flow field at various instants. Velocity vectors coloured by magnitude.

Scaling' technique (see Remark 14 in [49]) to emphasize the structure part by a factor of 5.0. The $S \rightarrow F \rightarrow FSI$ sequence is used in the computation. Figure 16 shows the mass balance and Figure 17 shows the flow field at various instants.

4.4. Abdominal aortic aneurysm

The arterial geometry used was created by making use of the image data found in [59, 60], with the arterial diameter and wall thickness coming from [61, 62]. The diameter of the artery segment is 3 cm at the inflow and 2 cm at the two outflow ends. The length is 14 cm and the size of the aneurysm is 6 cm. The problem geometry is shown in Figure 18. The pulsating inflow velocity profile as a function of time is not shown here but has the same form as that shown in Figure 2 in

DOI: 10.1002/fld

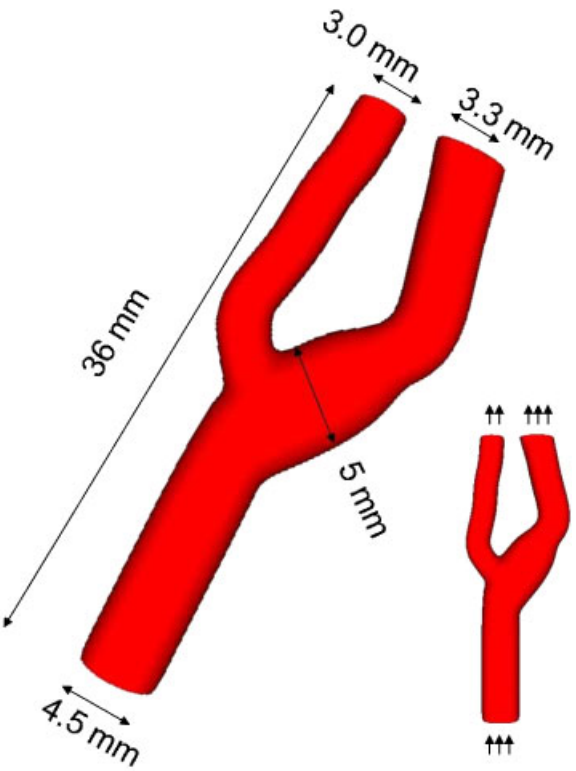

Figure 15. Carotid-artery bifurcation. Problem geometry.

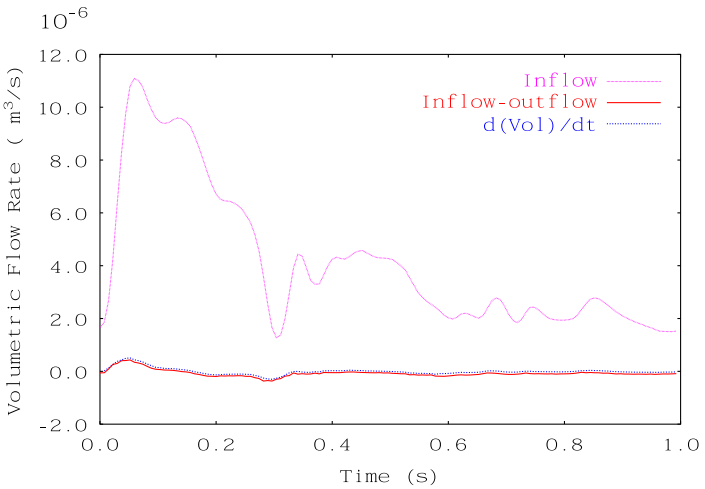

Figure 16. Carotid-artery bifurcation. Verification of mass balance. Volumetric inflow rate, difference between the volumetric inflow and outflow rates and rate of change for the artery volume.

DOI: 10.1002/fld

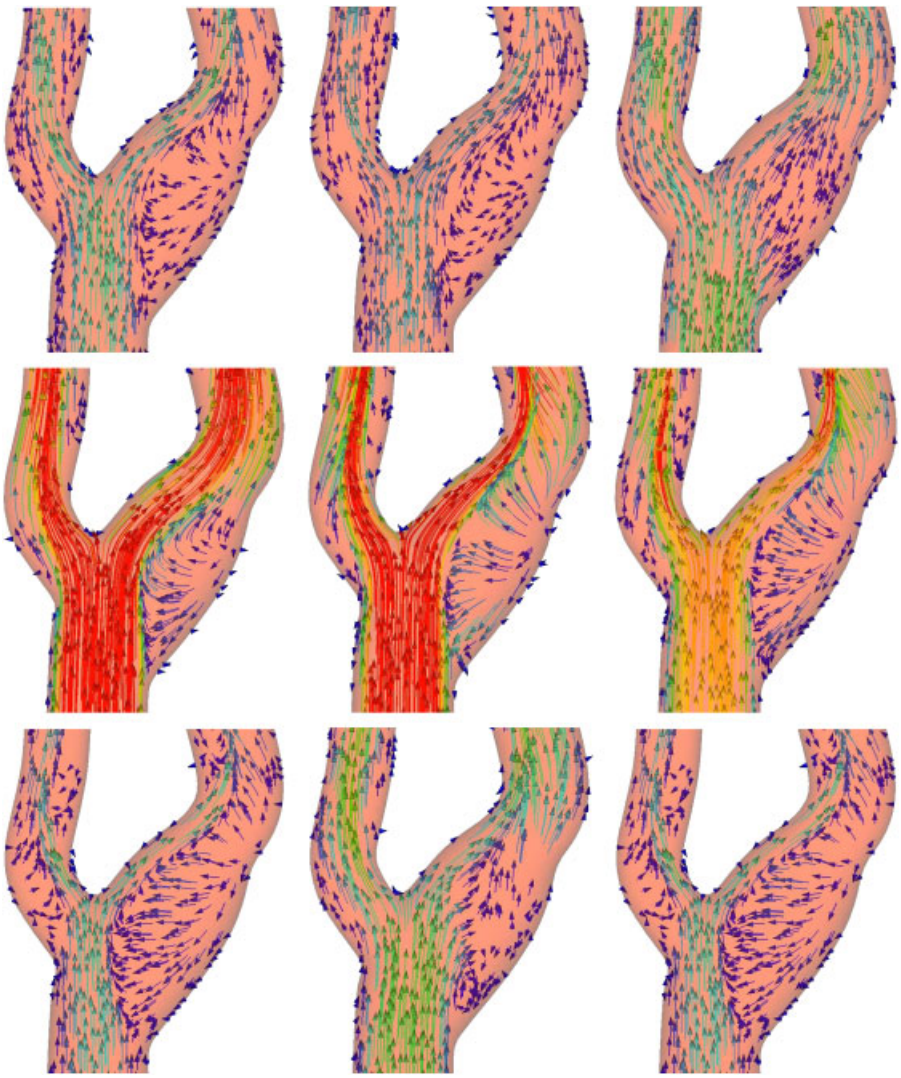

Figure 17. Carotid-artery bifurcation. Flow field at various instants. Velocity vectors coloured by magnitude.

Section 4.1. The minimum and maximum values are 0.13 and 1.13 m/s. The maximum value is based on the data found in [63]. The traction condition at the outflow boundaries is based on a NBP profile calculated in the way described in Section 3.2. That pressure profile is similar to the NBP profile given in Figure 3 in Section 4.1.1. The structural model is based on the membrane element. The wall thickness, stiffness and Poisson's ratio for the artery are 2.3 mm, 1.0×10^6 N/m^2 and 0.45, respectively.

The mesh for the artery consists of 6091 nodes and 12 072 three-node triangular elements. The fluid mechanics mesh contains 49 826 nodes and 295 687 four-node tetrahedral elements. The computations are carried out with the SSTFSI-SV technique (see Remarks 6 and 10 in [49]) and

DOI: 10.1002/fld

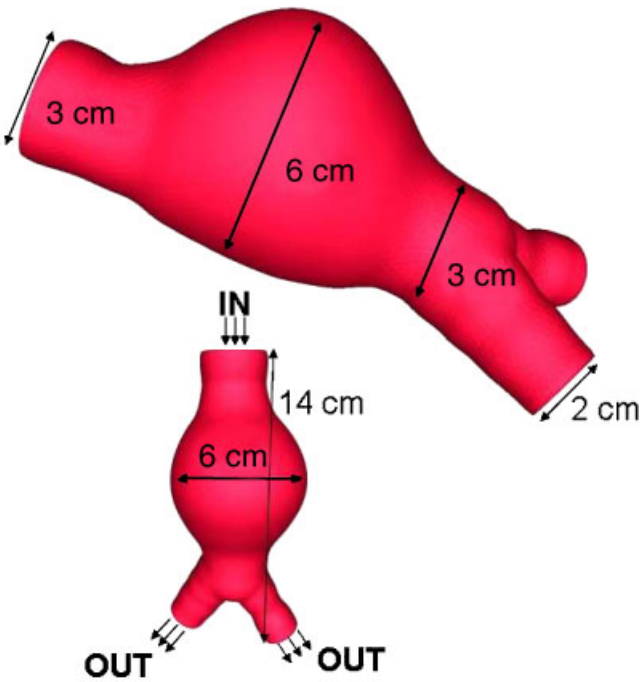

Figure 18. Abdominal aortic aneurysm. Problem geometry.

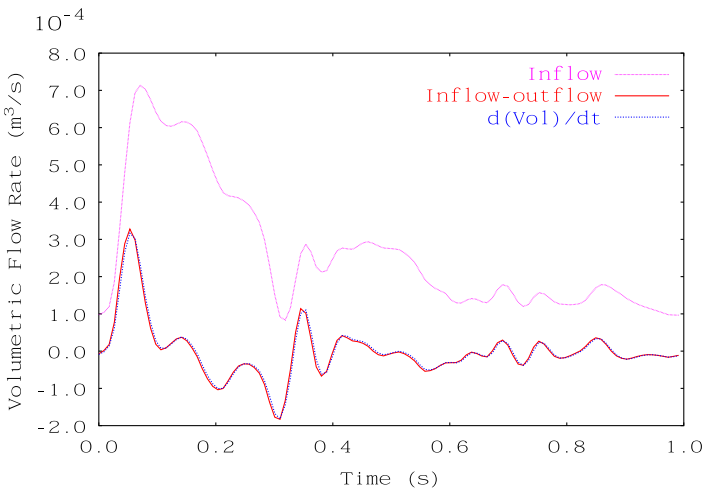

Figure 19. Abdominal aortic aneurysm. Verification of mass balance. Volumetric inflow rate, difference between the volumetric inflow and outflow rates and rate of change for the artery volume.

DOI: 10.1002/fld

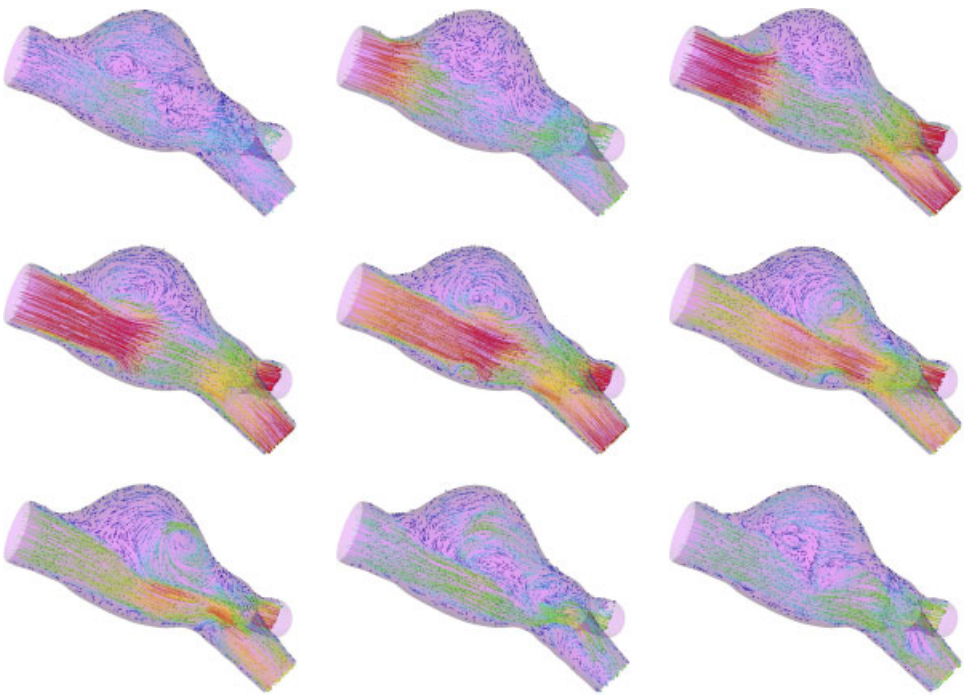

Figure 20. Abdominal aortic aneurysm. Flow field at various instants. Velocity vectors coloured by magnitude.

the SUPG test function option WTSE (see Remark 2 in [49]). The stabilization parameters used are those given by Equations (9)–(12) and Equations (14)–(17) in [49]. The damping coefficient η is set to $5.65 \times 10^3\,\mathrm{s}^{-1}$. The time-step size is 4.4×10^{-3} s. The number of nonlinear iterations per time step is 5, and the number of GMRES iterations per nonlinear iteration is 100. The $\mathrm{S} \rightarrow \mathrm{F} \rightarrow \mathrm{FSI}$ sequence is used in the computations.

Figure 19 shows the mass balance, and Figure 20 shows the flow field at various instants.

5. CONCLUDING REMARKS

This paper was intended to be a sequel to a recent paper [49], where new, enhanced versions of the deforming-spatial-domain/stabilized space–time (DSD/SST) and space–time fluid–structure interaction (FSI) techniques were introduced to increase the scope, accuracy, robustness and efficiency of these techniques. In the new stabilized space–time FSI (SSTFSI) techniques [49], the aspects of the FSI solution process enhanced include the DSD/SST formulation, the fluid–structure interface conditions, the preconditioning techniques used in iterative solution of the linear equation systems, and a contact algorithm protecting the quality of the fluid mechanics mesh between the structural surfaces coming into contact. A number of 3D numerical examples computed with the new SSTFSI techniques were also presented in [49]. Our objective in this paper was to extend the new SSTFSI techniques to FSI modelling in arterial fluid mechanics. We emphasized modelling

DOI: 10.1002/fld

of flow in arteries with aneurysm. The arterial structures can be modelled with the membrane or continuum elements, both of which are geometrically nonlinear, and the continuum element can be made of linearly elastic or hyperelastic (Mooney–Rivlin) material. We described here only the mathematical models and computational techniques that go beyond what was described in [49]. These additional topics were basically related to the structural modelling of the arteries. We presented test computations for cerebral and abdominal aortic aneurysms and carotid-artery bifurcation. The arterial geometries used in the computations were close approximations to the patient-specific image-based data. With the test computations presented, we showed that the new SSTFSI techniques can successfully deal with different types of arterial problems and structural models.

ACKNOWLEDGEMENTS

Portions of this work were supported by NIH/NHLBI Grant HL73868 (B.S. Conklin) and USDA 6250-51000-046 through the Children's Nutrition Research Center. We thank Mr. Fahad Saleh for generating the surface geometry of the carotid-artery segment reported in Section 4.

REFERENCES

1. Tezduyar TE. Stabilized finite element formulations for incompressible flow computations. *Advances in Applied Mechanics* 1992; **28**:1–44.
2. Tezduyar TE, Behr M, Liou J. A new strategy for finite element computations involving moving boundaries and interfaces—the deforming-spatial-domain/space–time procedure: I. The concept and the preliminary numerical tests. *Computer Methods in Applied Mechanics and Engineering* 1992; **94**:339–351.
3. Tezduyar TE, Behr M, Mittal S, Liou J. A new strategy for finite element computations involving moving boundaries and interfaces—the deforming-spatial-domain/space–time procedure: II. Computation of free-surface flows, two-liquid flows, and flows with drifting cylinders. *Computer Methods in Applied Mechanics and Engineering* 1992; **94**:353–371.
4. Mittal S, Tezduyar TE. Parallel finite element simulation of 3D incompressible flows—fluid–structure interactions. *International Journal for Numerical Methods in Fluids* 1995; **21**:933–953.
5. Kalro V, Tezduyar TE. A parallel 3D computational method for fluid–structure interactions in parachute systems. *Computer Methods in Applied Mechanics and Engineering* 2000; **190**:321–332.
6. Stein K, Benney R, Kalro V, Tezduyar TE, Leonard J, Accorsi M. Parachute fluid–structure interactions: 3-D computation. *Computer Methods in Applied Mechanics and Engineering* 2000; **190**:373–386.
7. Tezduyar T, Osawa Y. Fluid–structure interactions of a parachute crossing the far wake of an aircraft. *Computer Methods in Applied Mechanics and Engineering* 2001; **191**:717–726.
8. Ohayon R. Reduced symmetric models for modal analysis of internal structural-acoustic and hydroelastic-sloshing systems. *Computer Methods in Applied Mechanics and Engineering* 2001; **190**:3009–3019.
9. Tezduyar TE. Computation of moving boundaries and interfaces and stabilization parameters. *International Journal for Numerical Methods in Fluids* 2003; **43**:555–575.
10. Michler C, van Brummelen EH, Hulshoff SJ, de Borst R. The relevance of conservation for stability and accuracy of numerical methods for fluid–structure interaction. *Computer Methods in Applied Mechanics and Engineering* 2003; **192**:4195–4215.
11. Gerbeau J-F, Vidrascu M. A quasi-Newton algorithm based on a reduced model for fluid–structure interaction problems in blood flows. *Mathematical Modelling and Numerical Analysis* 2003; **37**:663–680.
12. Tezduyar TE, Sathe S, Keedy R, Stein K. Space–time techniques for finite element computation of flows with moving boundaries and interfaces. In *Proceedings of the III International Congress on Numerical Methods in Engineering and Applied Science*, Gallegos S, Herrera I, Botello S, Zarate F, Ayala G (eds), Monterrey, Mexico, CD-ROM, 2004.
13. Hubner B, Walhorn E, Dinkler D. A monolithic approach to fluid–structure interaction using space–time finite elements. *Computer Methods in Applied Mechanics and Engineering* 2004; **193**:2087–2104.
14. Michler C, van Brummelen EH, Hulshoff SJ, de Borst R. A monolithic approach to fluid–structure interaction. *Computers and Fluids* 2004; **33**:839–848.

DOI: 10.1002/fld

15. Tezduyar TE, Sathe S, Senga M, Aureli L, Stein K, Griffin B. Finite element modeling of fluid–structure interactions with space–time and advanced mesh update techniques. *Proceedings of the 10th International Conference on Numerical Methods in Continuum Mechanics* (*CD-ROM*), Zilina, Slovakia, 2005.
16. van Brummelen EH, de Borst R. On the nonnormality of subiteration for a fluid–structure interaction problem. *SIAM Journal on Scientific Computing* 2005; **27**:599–621.
17. Michler C, van Brummelen EH, de Borst R. An interface Newton–Krylov solver for fluid–structure interaction. *International Journal for Numerical Methods in Fluids* 2005; **47**:1189–1195.
18. Fernandez MA, Moubachir M. A Newton method using exact Jacobians for solving fluid–structure coupling. *Computers and Structures* 2005; **83**:127–142.
19. Gerbeau J-F, Vidrascu M, Frey P. Fluid–structure interaction in blood flow on geometries based on medical images. *Computers and Structures* 2005; **83**:155–165.
20. Tezduyar TE, Sathe S, Keedy R, Stein K. Space–time finite element techniques for computation of fluid–structure interactions. *Computer Methods in Applied Mechanics and Engineering* 2006; **195**:2002–2027.
21. Tezduyar TE, Sathe S, Stein K. Solution techniques for the fully-discretized equations in computation of fluid–structure interactions with the space–time formulations. *Computer Methods in Applied Mechanics and Engineering* 2006; **195**:5743–5753.
22. Bazilevs Y, Calo VM, Zhang Y, Hughes TJR. Isogeometric fluid–structure interaction analysis with applications to arterial blood flow. *Computational Mechanics* 2006; **38**:310–322.
23. Masud A, Khurram RA. A multiscale finite element method for the incompressible Navier–Stokes equations. *Computer Methods in Applied Mechanics and Engineering* 2006; **195**:1750–1777.
24. Khurram RA, Masud A. A multiscale/stabilized formulation of the incompressible Navier–Stokes equations for moving boundary flows and fluid–structure interaction. *Computational Mechanics* 2006; **38**:403–416.
25. Masud A. Effects of mesh motion on the stability and convergence of ALE based formulations for moving boundary flows. *Computational Mechanics* 2006; **38**:430–439.
26. Kuttler U, Forster C, Wall WA. A solution for the incompressibility dilemma in partitioned fluid–structure interaction with pure Dirichlet fluid domains. *Computational Mechanics* 2006; **38**:417–429.
27. Dettmer W, Peric D. A computational framework for fluid–rigid body interaction: finite element formulation and applications. *Computer Methods in Applied Mechanics and Engineering* 2006; **195**:1633–1666.
28. Tezduyar TE, Sathe S, Stein K, Aureli L. Modeling of fluid–structure interactions with the space–time techniques. In *Fluid–Structure Interaction*, Bungartz H-J, Schafer M (eds), Lecture Notes in Computational Science and Engineering, vol. 53. Springer: Berlin, 2006; 50–81.
29. Lohner R, Cebral JR, Yang C, Baum JD, Mestreau EL, Soto O. Extending the range of applicability of the loose coupling approach for FSI simulations. In *Fluid–Structure Interaction*, Bungartz H-J, Schafer M (eds), Lecture Notes in Computational Science and Engineering, vol. 53. Springer: Berlin, 2006; 82–100.
30. Wall WA, Gerstenberger A, Gamnitzer P, Forster C, Ramm E. Large deformation fluid–structure interaction—advances in ALE methods and new fixed grid approaches. In *Fluid–Structure Interaction*, Bungartz H-J, Schafer M (eds), Lecture Notes in Computational Science and Engineering, vol. 53. Springer: Berlin, 2006; 195–232.
31. Bletzinger K-U, Wuchner R, Kupzok A. Algorithmic treatment of shells and free form-membranes in FSI. In *Fluid–Structure Interaction*, Bungartz H-J, Schafer M (eds), Lecture Notes in Computational Science and Engineering, vol. 53. Springer: Berlin, 2006; 336–355.
32. Masud A, Bhanabhagvanwala M, Khurram RA. An adaptive mesh rezoning scheme for moving boundary flows and fluid–structure interaction. *Computers and Fluids* 2007; **36**:77–91.
33. Sawada T, Hisada T. Fluid–structure interaction analysis of the two dimensional flag-in-wind problem by an interface tracking ALE finite element method. *Computers and Fluids* 2007; **36**:136–146.
34. Wall WA, Genkinger S, Ramm E. A strong coupling partitioned approach for fluid–structure interaction with free surfaces. *Computers and Fluids* 2007; **36**:169–183.
35. Dettmer W, Peric D. A computational framework for fluid–structure interaction: finite element formulation and applications. *Computer Methods in Applied Mechanics and Engineering* 2006 (published online).
36. Torii R, Oshima M, Kobayashi T, Takagi K, Tezduyar TE. Influence of wall elasticity on image-based blood flow simulation. *Japan Society of Mechanical Engineers Journal Series A* 2004; **70**:1224–1231 (in Japanese).
37. Torii R, Oshima M, Kobayashi T, Takagi K, Tezduyar TE. Computation of cardiovascular fluid–structure interactions with the DSD/SST method. *Proceedings of the 6th World Congress on Computational Mechanics* (*CD-ROM*), Beijing, China, 2004.
38. Torii R, Oshima M, Kobayashi T, Takagi K, Tezduyar TE. Computer modeling of cardiovascular fluid–structure interactions with the deforming-spatial-domain/stabilized space–time formulation. *Computer Methods in Applied Mechanics and Engineering* 2006; **195**:1885–1895.

DOI: 10.1002/fld

39. Torii R, Oshima M, Kobayashi T, Takagi K, Tezduyar TE. Fluid–structure interaction modeling of aneurysmal conditions with high and normal blood pressures. *Computational Mechanics* 2006; **38**:482–490.
40. Torii R, Oshima M, Kobayashi T, Takagi K, Tezduyar TE. Influence of wall elasticity in patient-specific hemodynamic simulations. *Computers and Fluids* 2007; **36**:160–168.
41. Hughes TJR, Brooks AN. A multi-dimensional upwind scheme with no crosswind diffusion. In *Finite Element Methods for Convection Dominated Flows*, Hughes TJR (ed.), AMD-Vol.34. ASME: New York, 1979; 19–35.
42. Brooks AN, Hughes TJR. Streamline upwind/Petrov–Galerkin formulations for convection dominated flows with particular emphasis on the incompressible Navier–Stokes equations. *Computer Methods in Applied Mechanics and Engineering* 1982; **32**:199–259.
43. Tezduyar TE, Mittal S, Ray SE, Shih R. Incompressible flow computations with stabilized bilinear and linear equal-order-interpolation velocity–pressure elements. *Computer Methods in Applied Mechanics and Engineering* 1992; **95**:221–242.
44. Hughes TJR, Franca LP, Balestra M. A new finite element formulation for computational fluid dynamics: V. Circumventing the Babuška–Brezzi condition: a stable Petrov–Galerkin formulation of the Stokes problem accommodating equal-order interpolations. *Computer Methods in Applied Mechanics and Engineering* 1986; **59**:85–99.
45. Hughes TJR, Hulbert GM. Space–time finite element methods for elastodynamics: formulations and error estimates. *Computer Methods in Applied Mechanics and Engineering* 1988; **66**:339–363.
46. Tezduyar TE, Behr M, Mittal S, Johnson AA. Computation of unsteady incompressible flows with the finite element methods—space–time formulations, iterative strategies and massively parallel implementations. *New Methods in Transient Analysis*, PVP-Vol.246/AMD-Vol.143. ASME: New York, 1992; 7–24.
47. Johnson AA, Tezduyar TE. Mesh update strategies in parallel finite element computations of flow problems with moving boundaries and interfaces. *Computer Methods in Applied Mechanics and Engineering* 1994; **119**: 73–94.
48. Tezduyar TE. Finite element methods for flow problems with moving boundaries and interfaces. *Archives of Computational Methods in Engineering* 2001; **8**:83–130.
49. Tezduyar TE, Sathe S. Modeling of fluid–structure interactions with the space–time finite elements: solution techniques. *International Journal for Numerical Methods in Fluids*, in this issue.
50. Betsch P, Gruttmann F, Stein E. A 4-node finite shell element for the implementation of general hyperelastic 3d-elasticity at finite strains. *Computer Methods in Applied Mechanics and Engineering* 1996; **130**:57–79.
51. Stuparu M. Human heart valves. Hyperelastic material modeling. *Proceedings of the X-th Conference on Mechanical Vibrations*, Timisoara, Romania, 2002.
52. Saad Y, Schultz M. GMRES: a generalized minimal residual algorithm for solving nonsymmetric linear systems. *SIAM Journal on Scientific and Statistical Computing* 1986; **7**:856–869.
53. Womersley JR. Method for the calculation of velocity, rate of flow and viscos drag in arteries when the pressure gradient is known. *Journal of Physiology* 1955; **127**:553–563.
54. Otto F. Die grundform des arteriellen pulses. *Zeitung fur Biologie* 1899; **37**:483–586.
55. Piersol NE, Lee S, Kalata W, Loth F, Fischer PF, Leaf G, Alperin N, Bassiouny HS. Automated simulation of velocity and wall shear stress patterns inside a healthy carotid bifurcation. http://web.mit.edu/selee/www/menu1/research/healthy_carotid.html
56. Krejza J, Arkuszewski M, Kasner SE, Weigele J, Ustymowicz A, Hurst RW, Cucchiara BL, Messe SR. Carotid artery diameter in men and women and the relation to body and neck size. *Stroke* 2006; **37**:1103–1105.
57. http://www.hopkinsmedicine.org/Press_releases/2004/11_09c_04.html
58. Edwards M. Carotid arteries: use of ultrasound duplex imaging for detection of plaque. http://test.cvtcollege.org/Ac_Programs/dms_vascular/studentmisty.html
59. http://www.vascularweb.org/_CONTRIBUTION_PAGES/Patient_Information/3_Most_Common_AVA/AorticAneurysms_AVA.html
60. http://www.slrsurgery.org/divisions/vascular.html
61. http://www.camsf.com/vasc_aortic.html
62. Li AE, Kamel I, Rando F, Anderson M, Lima JAC, Kumbasar B, Bluemke DA. Using MRI to assess aortic wall thickness in the multiethnic study of atherosclerosis: distribution by race, sex, and age. *American Journal of Roentgenology* 2004; **182**:593–597.
63. Rowland T, Potts J, Potts T, Son-Hing J, Harbison G, Sandor G. Cardiovascular responses to exercise in children and adolescents with myocardial dysfunction. *American Heart Journal* 1999; **137**:126–133.

DOI: 10.1002/fld